RESEARCH ARTICLE SUMMARY

ULTRAFAST MICROSCOPY

Ultrafast vector imaging of plasmonic skyrmion dynamics with deep subwavelength resolution

Timothy J. Davis*, David Janoschka, Pascal Dreher, Bettina Frank, Frank-J. Meyer zu Heringdorf*, Harald Giessen*

INTRODUCTION: Topology is the study of geometric properties that are unaffected by continuous changes in shape and size. Skyrmions are examples of topological defects in vector fields. Skyrmions exhibit a characteristic vector structure. When excited by electromagnetic near fields on thin metal films, they are called plasmonic skyrmions. These fields exist at sub–100-nm scales and oscillate with periods of a few femtoseconds and thus are difficult to measure.

RATIONALE: Two-photon photoemission electron microscopy studies were previously able to image the local plasmon fields with femtosecond time resolution, but the vector information of the local electric fields was missing. Here we introduce a new technique, time-resolved vector microscopy, that enables us to compose entire movies on a subfemtosecond time scale and a 10-nm spatial scale of the electric field vectors of surface plasmon polaritons (SPPs). We use this technique to image complete time sequences of propagating surface plasmons, demonstrating their spin-momentum locking, as well as plasmonic skyrmions on atomically flat single-crystalline gold films that have been patterned using gold ion beam lithography.

RESULTS: The key technique to obtain vector information is to take two sequences of the entire process with two different probe beam polarizations. Hence, the electric field vectors will be projected onto the probing electric field by the two-photon photoemission process. The spatial dependence of the two in-plane vector components coupled with Maxwell's equations then permits the retrieval of the out-of-plane component. This allows us to unambiguously resolve all vector components of the electric field as well as their time dynamics, enabling the retrieval of the experimental time-dependent skyrmion number and indicating the periodic transformation from skyrmion number +1 to −1 and back on a time scale of a few femtoseconds. Additionally, all three magnetic field vectors of the surface can be obtained from the electric field vectors by using Maxwell's curl equation.

ON OUR WEBSITE

Read the full article at https://dx.doi.org/10.1126/science.aba6415

CONCLUSION: With our vector microscopy technique, we are able to image plasmonic spin-momentum locking and plasmonic skyrmion dynamics. In the future, other topological nanophotonic systems should be in reach as well; these include plasmonic merons or short-range skyrmions, where the dispersion of plasmons in extremely thin films is used. This research will open the door to creating linear optical features on the few-nanometer length scale. ■

The list of author affiliations is available in the full article online.
*Corresponding author. Email: timd@unimelb.edu.au (T.J.D.); meyerzh@uni-due.de (F.-J.M.z.H.); giessen@pi4.uni-stuttgart.de (H.G.)
Cite this article as T. J. Davis *et al.*, *Science* **368**, eaba6415 (2020). DOI: 10.1126/science.aba6415

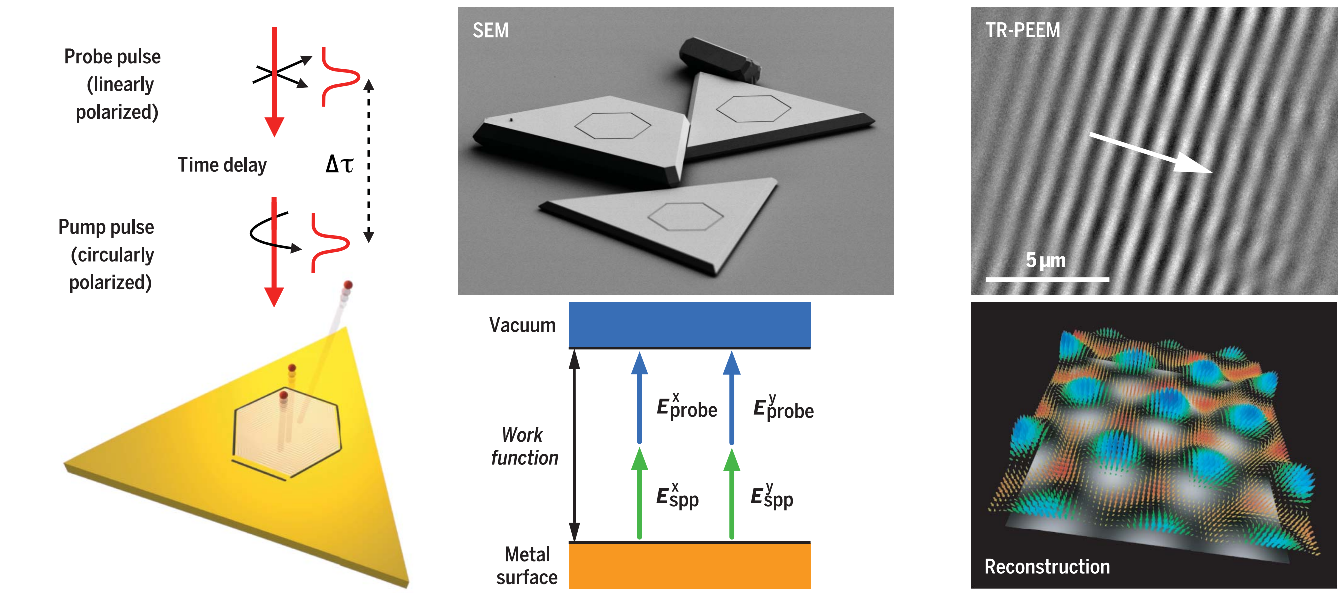

Ultrafast time-resolved vector microscopy of plasmonic skyrmions. Femtosecond laser pump-probe techniques using polarized beams combined with two-photon electron emission in an electron microscope enables the retrieval of all vector components of the electric field of propagating SPPs as a function of time. We used this technique to image the vectorial time dynamics of the plasmonic skyrmion field. Hexagons are milled into single-crystalline gold flakes via ion beam lithography. A circularly polarized femtosecond laser pulse excites surface plasmon waves on the gold flakes that interfere to create an SPP skyrmion lattice. The SPPs are detected by interference with a second laser pulse that is first polarized in the *x* direction to retrieve the E_x component of the SPP wave and then is polarized in the *y* direction to produce the E_y component. These fields are combined to obtain the characteristic in-plane pattern of the skyrmion lattice: $E_{||}$. Use of the measured field components in Maxwell's equations enables the vertical field component E_z to be calculated. From these data, we reconstruct the vector field of the SPP skyrmion and, by varying the laser pump-probe delay time (Δτ), gain time-resolved information (top right), allowing us to create vector movies that show plasmonic spin-momentum locking and plasmonic skyrmions (bottom right). SEM, scanning electron microscopy; TR-PEEM, time-resolved photoemission electron microscopy.

RESEARCH ARTICLE

ULTRAFAST MICROSCOPY

Ultrafast vector imaging of plasmonic skyrmion dynamics with deep subwavelength resolution

Timothy J. Davis[1,2,3]*, David Janoschka[2], Pascal Dreher[2], Bettina Frank[3], Frank-J. Meyer zu Heringdorf[2]*, Harald Giessen[3]*

Plasmonic skyrmions are an optical manifestation of topological defects in a continuous vector field. Identifying them requires characterization of the vector structure of the electromagnetic near field on thin metal films. Here we introduce time-resolved vector microscopy that creates movies of the electric field vectors of surface plasmons with subfemtosecond time steps and a 10-nanometer spatial scale. We image complete time sequences of propagating surface plasmons as well as plasmonic skyrmions, resolving all vector components of the electric field and their time dynamics, thus demonstrating dynamic spin-momentum coupling as well as the time-varying skyrmion number. The ability to image linear optical effects in the spin and phase structures of light in the single-nanometer range will allow for entirely novel microscopy and metrology applications.

Skyrmions (1, 2) in magnetic films were predicted some time ago (3, 4) and were observed recently in neutron scattering experiments (5), with the topological nature of the phase confirmed in subsequent Hall measurements (6). These phenomena have been observed in other magnetic materials (7–11), and clusters of them have been created in isolated regions in liquid crystals (12). Images of skyrmion lattices and the reconstruction of their spatial magnetization distribution have been obtained using Lorentz-force electron microscopy (13). Skyrmion vector fields in three-dimensional (3D) systems form knotted structures that could, in principle, be generated by light fields (14). In the field of optics, artificial skyrmions in two dimensions have been formed by interfering surface plasmon polaritons (SPPs) on gold metal films (15–18). Such SPP skyrmions have potential as a model system for increasing our understanding of their dynamics. Skyrmions are inherently vectorial in nature, as is evident in the spin structure of magnetic skyrmions and in the vector character of the electric fields in SPP skyrmions. Complete identification and analysis of skyrmions in experiments requires a full determination of their vectorial fields, and observing their dynamical behavior requires temporal information. Such information is usually not available, apart from the results of some complex time-resolved scanning near-field optical microscopy experiments (19–22). In this study, we use time-resolved vector microscopy to retrieve the entire spatiotemporal vector dynamics of SPP skyrmions with nanometer spatial and femtosecond time resolution.

[1]School of Physics, University of Melbourne, Parkville, Victoria 3010 Australia. [2]Faculty of Physics and Center for Nanointegration, Duisburg-Essen (CENIDE), University of Duisburg-Essen, 47048 Duisburg, Germany. [3]4th Physics Institute, Research Center SCoPE, and Integrated Quantum Science and Technology Center, University of Stuttgart, 70569 Stuttgart, Germany.
*Corresponding author. Email: timd@unimelb.edu.au (T.J.D.); meyerzh@uni-due.de (F.-J.M.z.H.); giessen@pi4.uni-stuttgart.de (H.G.)

Two-photon photoemission

The technique we use to measure the SPP electric fields is based on a two-photon photoemission (2PPE) process (Fig. 1A). A pump light pulse from a 16-fs Ti:sapphire laser source, normally incident on a single-crystal gold surface, excites SPPs from grooves etched by ion beam milling (Fig. 1, B and C) to subsequently generate a plasmonic skyrmion field. The SPPs propagate over the surface and interfere with the electric field of a probe pulse that arrives after a delay $\Delta\tau$. The interference between the probe field and the surface plasmon field is responsible for the position-dependent electron emission via a two-photon process (Fig. 2A). The experiment takes place in a photoemission electron microscope (PEEM) that forms an image of the emission points of the photoelectrons, yielding a visualization of the surface plasmon wave (23). The femtosecond laser has a repetition rate of 80 MHz, resulting in a large number of repeated measurements on the sample, thus enabling us to obtain accurate image statistics of the electron emission. Repeating this process for a series of different pump-probe delays provides temporal information about the motion of the SPP over the surface that allows the dynamics of SPP propagation and interference to be studied (24). Such 2PPE-PEEM techniques have been used to investigate the orbital angular momentum and focusing properties of SPPs (25, 26).

These normal-incidence pump-probe measurements used to be performed with the same polarization for the pump and the probe (23)—e.g., right circular polarization (RCP) for the pump and RCP for the probe. This method yields only one in-plane component of the SPP electric field. However, for vector microscopy, at least two linearly independent vector components, such as E_x and E_y, are required. We therefore record two independent pump-probe sequences using two orthogonal probe polarizations that measure the SPP field strength in two orthogonal directions. Interference between the E^x_{spp} and the E^x_{probe} field yields information about the x vectorial component by 2PPE. The same holds true for

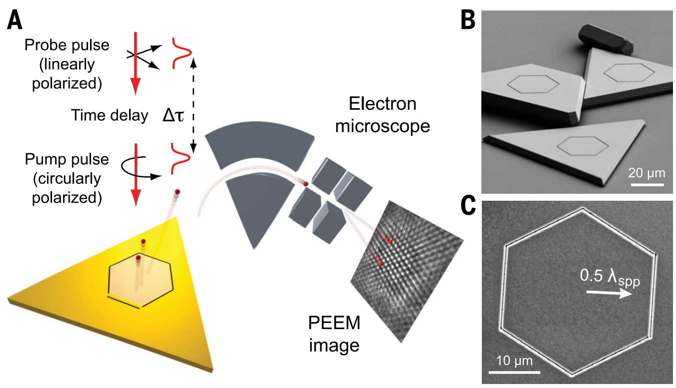

Fig. 1. 2PPE-PEEM process used to obtain vector and time information from surface plasmons. (**A**) The 2PPE-PEEM process involves a pump-probe excitation of surface plasmons from grooves etched in a single-crystal gold flake, the interference of the propagating surface plasmon with a probe pulse, and the subsequent imaging of the ejected photoelectrons in a photoemission electron microscope. The pulse duration is typically 16 fs, and the delay time ($\Delta\tau$) is varied in steps of 0.16 fs. (**B**) Scanning electron microscopy image showing examples of single-crystal gold flakes and the hexagonal boundary shapes milled by an ion beam. (**C**) The hexagonal boundary milled into a single-crystal gold flake, as imaged in the electron microscope. The arrow points to the side that is displaced by a half wavelength of the SPP (λ_{spp}) to create the skyrmion lattice.

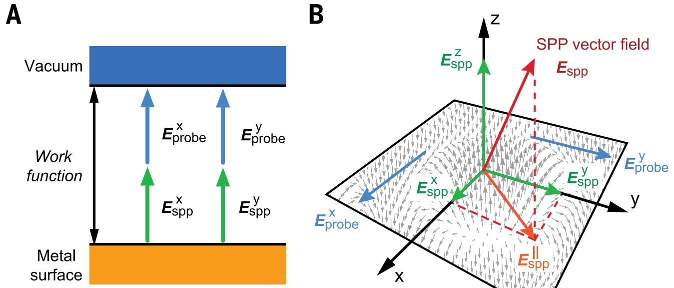

Fig. 2. Method for extracting vector information from the 2PPE-PEEM experiment. (**A**) The excitation of photoelectrons involves a two-photon process to overcome the work function of the metal film. A submonolayer of cesium is deposited on the gold surface to reduce the work function below 3 eV to facilitate the two-photon absorption. The polarization direction of the probe pulse determines the component of the SPP electric field that is measured. (**B**) Vector fields in the plane of the SPP are obtained from the interference between the orthogonal probe fields during two separate measurements. From the spatial dependence of these two vectors, we derive the out-of-plane vector.

the respective y vectorial components of E^y_{spp} with the E^y_{probe} (Fig. 2A). See fig. S1 for a depiction of the optical setup with different polarizers and waveplates. The experimental data hence enable us to reconstruct the 2D vector structure $\mathbf{E}^{\parallel}_{\mathrm{spp}}$ of the SPP as a function of time with a spatial resolution of 10 nm, as determined by the microscope electron optics, and a time resolution better than 0.2 fs, set by the short-term stability of the pump-probe laser system. The two-photon emission process depends on the square of the total electric field intensity at the surface, which consists of the vectorial sum of the light field $\mathbf{E}_{\mathrm{probe}}$ of the probe and the surface plasmon electric field $\mathbf{E}_{\mathrm{spp}}(\mathbf{r})$. When the probe field uniformly illuminates the metal surface, the spatial dependence of the electron emission arises only from the SPP field. When the SPP electric field is much weaker than that of the probe, the two-photon absorption depends on

$$I^2(\mathbf{r}) = |\mathbf{E}_{\mathrm{probe}} + \mathbf{E}_{\mathrm{spp}}(\mathbf{r})|^4 \approx I^2_{\mathrm{probe}} + 4I_{\mathrm{probe}}\mathrm{Re}\left(\mathbf{E}^*_{\mathrm{probe}} \cdot \mathbf{E}_{\mathrm{spp}}(\mathbf{r})\right)$$

which is linear in the SPP field. Here, I^2 is the intensity (squared) of the electric field, I_{probe} is the intensity of the probe pulse, and $\mathbf{E}^*_{\mathrm{probe}}$ is the complex conjugate of the probe electric field. For such weak SPP fields, the nonlinear emission is dominated by the projection of the SPP field vector on the probe light field vector, which is oriented within the surface plane (*27–29*) (Fig. 2B). Having retrieved E^x_{spp} and E^y_{spp} as described, the final unknown component perpendicular to the surface is calculated from Maxwell's equations. Just above the metal surface, there are no free charges and the divergence of the SPP field is zero: $\nabla \cdot \mathbf{E}_{\mathrm{spp}} = 0$. From this relation, we obtain the gradient of the vector field component $\partial E^z_{\mathrm{spp}}/\partial z = -\partial E^x_{\mathrm{spp}}/\partial x - \partial E^y_{\mathrm{spp}}/\partial y$ out of the plane, as the position dependence of both $E^x_{\mathrm{spp}}(\mathbf{r})$ and $E^y_{\mathrm{spp}}(\mathbf{r})$ is known from the experiment. The SPP electric field decays exponentially with distance above the metal surface, approximately as $\exp(-\gamma z)$, where γ is a known parameter that depends on the incident light central wavelength (800 nm) and the electric permittivity of the metal (*29*). With this position dependence, we obtain $E^z_{\mathrm{spp}} \approx -(1/\gamma)\,\partial E^z_{\mathrm{spp}}/\partial z$. Once we have the three vector components of the electric field and their time variation, we can deduce many other properties of the SPP field. All vector components of the SPP magnetic field ($\mathbf{B}$) can be found from the relation $\nabla \times \mathbf{E} = -\partial \mathbf{B}/\partial t$ and integrating over time (t). The SPP surface charge is proportional to the normal component E^z_{spp} of the electric field $\sigma_{\mathrm{spp}}(\mathbf{r},t) = (\epsilon_0 - \epsilon_{\mathrm{m}})E^z_{\mathrm{spp}}(\mathbf{r},t)$, which depends on the difference between the electric permittivity of the vacuum ϵ_0 and that of the metal ϵ_{m}. Therefore, the normal component E^z_{spp} gives a representation of the SPP surface charge as a function of position and time. The rotation of the SPP electric field in time represents classical spin $\mathbf{s}$, which is a vector normal to the polarization ellipse swept out by the electric field vector (*30*). For time-dependent real fields, the classical spin has a direction $\mathbf{s} = (\mathbf{E}(\mathbf{r},t) \times \partial\mathbf{E}(\mathbf{r},t)/\partial t)/\omega|\mathbf{E}|^2$, where ω is the center frequency of the light pulses (as derived in the fig. S4 and eqs. S11 to S16). Thus, from our experimental measurements we obtain almost complete information about the SPP surface charge, including the spatial and temporal properties of the electric and magnetic fields it produces, lacking only the overall magnitude of the field.

Experimental results

We first test our vector measurement technique on a plane-wave SPP (Fig. 3). A single-crystal gold flake, which is 80 to 100 μm wide, is chemically grown on silicon (*31*). The flake is

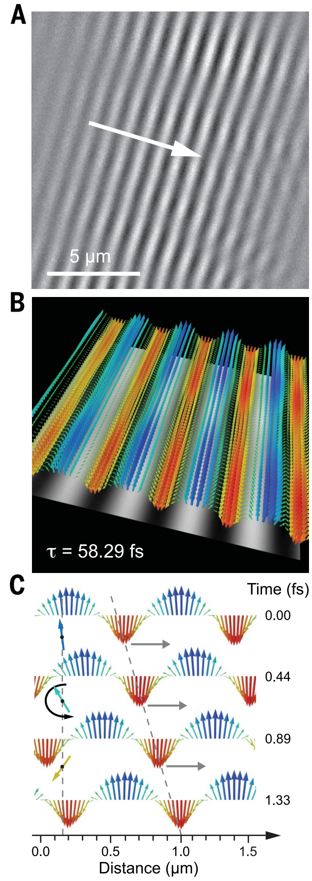

Fig. 3. 2PPE-PEEM measurement of the time evolution of the electric field vectors of an SPP traveling wave. (**A**) An image of the wave taken at one pump-probe delay time. The arrow shows the wave propagation direction. A time-invariant background signal has been removed using a differencing procedure described in the supplementary text (section II). (**B**) Full vectorial reconstruction of the SPP electric field at the pump-probe time delay τ = 58.29 fs. The image beneath the vectors shows the vertical component of the SPP electric field that is proportional to the SPP surface charge (white, positive; black, negative), whereas the PEEM image (A) probes the in-plane component of the plasmon field. See Movie 1. (**C**) Four profiles through the experimental wavefront depicting the SPP vector configurations at different relative time delays. The sloped dashed line and gray arrows highlight the propagation of the wavefront with time associated with the SPP traveling wave. The vertical dashed line and blue, cyan, and yellow arrows highlight the rotation of the SPP electric field vector at one position in space that gives rise to transverse spin.

then placed in an ion beam lithography system where a groove is milled using Au^{2+} ions. A pump pulse with an 800-nm center wavelength and a 16-fs pulse duration that is linearly polarized perpendicular to the groove uniformly illuminates the gold flake and excites a long-range surface plasmon of wavelength 780 nm

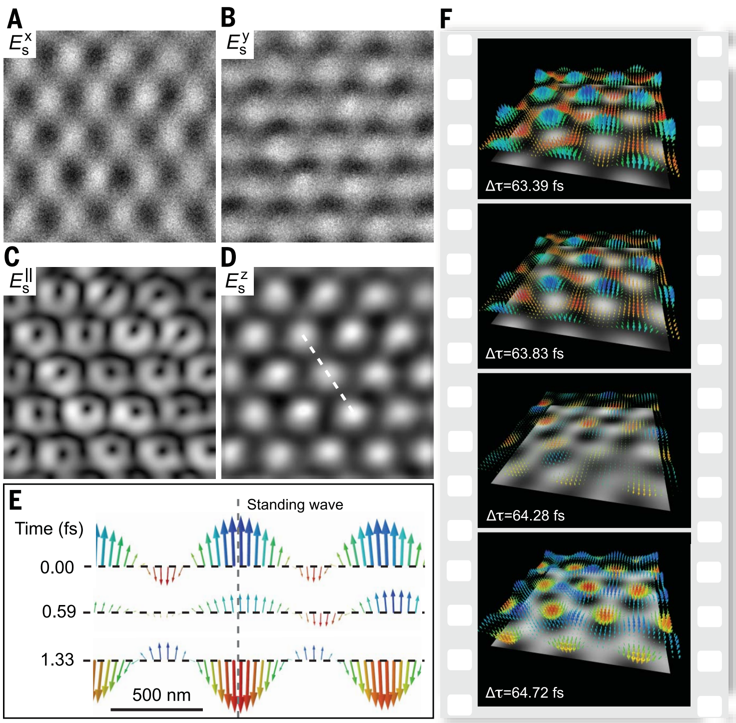

Fig. 4. Vector and time measurement of the SPP skyrmions. (**A** and **B**) Two images taken at the same pump-probe delay times but with orthogonal polarization states of the probe field. A time-stationary background has been removed, as described in the supplementary text (section II). (**C** and **D**) The in-plane $E_s^{||} = \sqrt{E_s^{x^2} + E_s^{y^2}}$ and out-of-plane E_s^z components of the SPP skyrmion field extracted from the experimental data. (**E**) Experimentally derived vectors along the dashed line in (D) for three relative time delays. The vertical dashed line highlights the standing wave nature of the SPP field at this location. (**F**) Time dependence of the SPP skyrmion lattice, as obtained from experiment (Movie 2). The background image is scaled to the normal component, which provides a representation of the SPP surface charge (white, positive; black, negative; gray, zero).

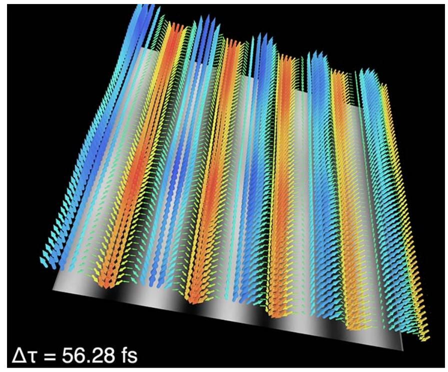

Movie 1. Vector dynamics of the propagating SPPs.

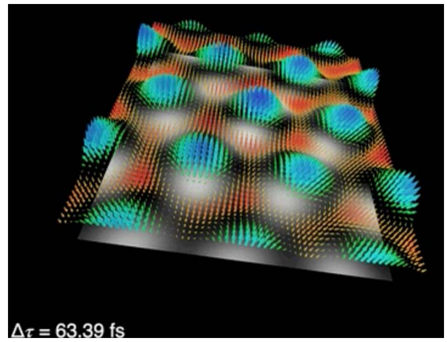

Movie 2. Vector dynamics of the spinning plasmonic skyrmion electric field vectors.

that propagates from the boundary (Fig. 3A). For the first series of measurements, the electron emission image is obtained at each time delay with the probe pulse linearly polarized in the direction of SPP propagation. We obtain a vector representation of the SPP field as in Fig. 3B. Four profiles of the field through the wavefront at different pump-probe delay times are shown in Fig. 3C. The experimentally measured SPP vectors exhibit the well-known in-plane rotation of the plane wave SPP field associated with transverse spin (*32*–*34*). The time-dependent vector field is shown in Movie 1 and in the supplementary materials (movies S1 to S3).

In the second experiment, a plasmonic vector skyrmion field is created using grooves milled into the gold flake (Fig. 1C), forming a hexagon boundary where SPPs are excited. One side of the hexagon is displaced by 390 nm, half of an SPP wavelength, which is necessary to generate a hexagonal lattice of SPP skyrmions (*16*). Two image frames at the same delay time but orthogonal polarizations are shown in Fig. 4, A and B. A constant background has been removed by subtracting images from the same time sequence but delayed by a half cycle (1.33 fs), as discussed in supplementary text section II. To reduce the noise associated with the detection of the electrons in the experiment, the images are smoothed with a low-pass filter. This filtering improves the numerical calculation of the derivatives required to obtain the normal component of the SPP field but reduces the spatial resolution to ~1/10 of the SPP wavelength. Once the x and y components of the field and their spatial variations are measured, it is straightforward to extract the in-plane component $E_s^{||}$ (Fig. 4C) and the vertical component E_s^z (Fig. 4D) of the SPP skyrmion field.

With the vector data, we create a 3D rendering of the SPP vectors (Fig. 4F) that shows the distinctive skyrmion field evolving in time, owing to the standing wave pattern of the SPPs from the six grooves in the metal flake. In Movie 2 and the supplementary materials (movies S4 to S6), we show a complete time sequence of the experimentally measured vectors. The lengths of the vectors correspond to the magnitude of the electric field, and the color codes the direction out of the plane. Figure 4E depicts sections through the SPP skyrmions at three different pump-probe delay times. The SPP field vector rotates out of the plane of the metal surface (dashed line in Fig. 4E) close to the skyrmion center. This rotation leads to two distinct patterns at time delays equal to a half-wave cycle, corresponding to pump-probe delay times of Δτ = 63.39 and 64.72 fs; these patterns are associated with skyrmion numbers of opposite sign. One might think that these two configurations of vectors represent a skyrmion-antiskyrmion pair (*35*); however, in our case, we believe that the configurations simply indicate the electric field reversal after half of an optical cycle. The magnetic flux associated with the SPP skyrmion can be retrieved from the electric field (as shown in fig. S3) and is similar to that observed in a skyrmion lattice in $Fe_{0.5}Co_{0.5}Si$ using electron holography (*36*).

Identifying skyrmion type

Three basic skyrmion types have been observed experimentally in solid-state systems, revealing the different ways that the field vector rotates with position through the center of the skyrmion. The vector formation is either Néel type (*37*) or Bloch type (*13*, *38*), which in solid-state systems depends on the boundary and symmetry conditions. Néel skyrmions reveal a cycloidic vector rotation, whereas Bloch skyrmions are

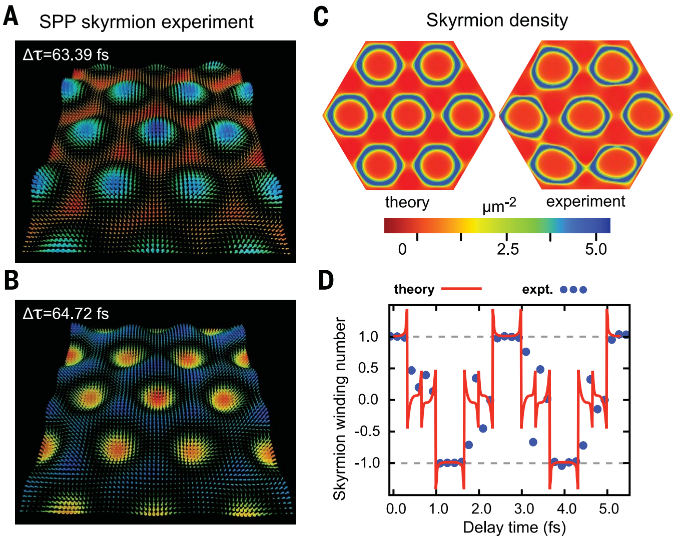

Fig. 5. Skyrmion number density. (**A** and **B**) Regions of the SPP skyrmion lattice at extrema of the SPP wave cycle, at times equivalent to a π phase shift. (**C**) The skyrmion number density $\mathcal{N}_s$ is calculated from the data in (A) and compared with a theoretical calculation. The color codes the density and is slightly negative in the red regions (≈−0.05 μm^{-2}) and peaks just above 5 μm^{-2} in the blue regions. (**D**) The skyrmion winding number $\mathcal{W}$ per skyrmion for the regions in (C) is obtained from the experiment for two complete SPP wave periods. At the extrema, the winding number is ±1, with the minus sign indicating that the SPP skyrmion vector rotates over a complete sphere but in the opposite sense. The theoretical curve is calculated from an analytical model of interfering SPP waves (see supplementary text section V for details).

characterized by a helical flip inverting their field vectors. Antiskyrmions with a quadrupolar field orientation were observed (*39*) in tetragonal Heusler materials. In this case, the cylindrical symmetry is broken and the antiskyrmion field displays a combination of cycloidic and helical vector behavior. It is clear that the SPP skyrmions in Fig. 4 are of the Néel type.

The topological nature of skyrmion vector fields is characterized by integer skyrmion numbers derived from the skyrmion number density (*2*)

$$\mathcal{N}_s(\mathbf{r}) = \frac{1}{4\pi}\hat{e}\cdot\left(\frac{\partial\hat{e}}{\partial x}\times\frac{\partial\hat{e}}{\partial y}\right)$$

This density depends on the unit vectors $\hat{e}(\mathbf{r},t) = \mathbf{E}(\mathbf{r},t)/E(\mathbf{r},t)$ of the electric fields, which are functions of time. Figure 5, A and B, shows the SPP skyrmions at times Δτ = 63.39 and 64.72 fs, separated by half of a time cycle. The skyrmion number density for the lattice in Fig. 5A is depicted in Fig. 5C. The theoretical number density is calculated using a simple wave model of the fields in the lattice, as discussed in supplementary text section V. The skyrmion number density obtained from experiment at the maximum of the SPP wave cycle (Fig. 5A) corresponds closely to the theoretical values. The skyrmion number or winding number $\mathcal{W} = \int_S \mathcal{N}_s dA$ is the integral of the number density over the surface (here, A is the area of the unit cell). This number equals the number of times the direction of the vector field rotates around a whole sphere (*2*) as we traverse the gold surface. In our case, the skyrmion array is finite and decays with increasing distance from the center of the pattern, which requires us to match the boundary of the integration area S to the hexagonal lattice. For the number density of Fig. 5C, the experimental skyrmion number is $\mathcal{W} = 6.93$, which is close to the theoretical value of $\mathcal{W} = 7$, corresponding to seven skyrmions in the integration region. Our time-resolved technique allows us to extract the skyrmion number $\mathcal{W}/7$ for this area as a function of time delay (Fig. 5D) for two cycles of the SPP standing wave. For an appreciable fraction of the first half of the SPP wave cycle, $\mathcal{W}/7 \approx 1$ as expected. During the second half of the cycle, $\mathcal{W}/7 \approx -1$, corresponding to a reverse winding of the SPP vectors across the surface.

Outlook

Our time-resolved vector microscope should be able to reveal many phenomena associated with spin-photon coupling, the photonic spin-Hall effect, and orbital angular momentum physics. Furthermore, it should be possible to use plasmons with strongly reduced wavelengths in 20-nm-thick gold films (*26*) to obtain short-range skyrmions. Such structures would allow for extremely small spin and phase structures of the light fields (*17*) down to the single-nanometer range and might be used for novel microscopy and metrology applications (*40*, *41*). The intense fields created by femtosecond laser pulses have the potential to induce nonlinear behavior in optical materials supporting surface plasmons, such as thin graphene films or metals overcoated with materials exhibiting Kerr nonlinearities. SPP skyrmions in such materials could exhibit solitonic properties and might interact with other SPP waves, through the nonlinearity of the material. Such systems could, in principle, enable scattering of SPPs and SPP skyrmions on each other and trigger a plethora of nonlinear nanooptical effects. Finally, such nanostructures could be used in photon-induced near-field electron microscopy (*42*, *43*) and electron energy-loss spectroscopy (*44*) experiments, in which electrons and light fields take on different roles.

REFERENCES AND NOTES

1. T. H. R. Skyrme, A unified field theory of mesons and baryons. *Nucl. Phys.* **31**, 556–569 (1962). doi: 10.1016/0029-5582(62)90775-7
2. K. Everschor-Sitte, M. Sitte, Real-space Berry phases: Skyrmion soccer (invited). *J. Appl. Phys.* **115**, 172602 (2014). doi: 10.1063/1.4870695
3. A. N. Bogdanov, D. A. Yablonskii, Thermodynamically stable "vortices" in magnetically ordered crystals. The mixed state of magnets. *Sov. Phys. JETP* **68**, 101–103 (1989).
4. U. K. Rössler, A. N. Bogdanov, C. Pfleiderer, Spontaneous skyrmion ground states in magnetic metals. *Nature* **442**, 797–801 (2006). doi: 10.1038/nature05056; pmid: 16915285
5. S. Mühlbauer *et al.*, Skyrmion lattice in a chiral magnet. *Science* **323**, 915–919 (2009). doi: 10.1126/science.1166767; pmid: 19213914
6. A. Neubauer *et al.*, Topological Hall effect in the A phase of MnSi. *Phys. Rev. Lett.* **102**, 186602 (2009). doi: 10.1103/PhysRevLett.102.186602; pmid: 19518895
7. W. Münzer *et al.*, Skyrmion lattice in the doped semiconductor $Fe_{1-x}Co_xSi$. *Phys. Rev. B* **81**, 041203 (2010). doi: 10.1103/PhysRevB.81.041203
8. K. Shibata *et al.*, Towards control of the size and helicity of skyrmions in helimagnetic alloys by spin-orbit coupling. *Nat. Nanotechnol.* **8**, 723–728 (2013). doi: 10.1038/nnano.2013.174; pmid: 24013133
9. C. Pfleiderer *et al.*, Skyrmion lattices in metallic and semiconducting B20 transition metal compounds. *J. Phys. Condens. Matter* **22**, 164207 (2010). doi: 10.1088/0953-8984/22/16/164207; pmid: 21386413
10. G. Berruto *et al.*, Laser-Induced Skyrmion Writing and Erasing in an Ultrafast Cryo-Lorentz Transmission Electron Microscope. *Phys. Rev. Lett.* **120**, 117201 (2018). doi: 10.1103/PhysRevLett.120.117201; pmid: 29601740
11. N. Nagaosa, Y. Tokura, Topological properties and dynamics of magnetic skyrmions. *Nat. Nanotechnol.* **8**, 899–911 (2013). doi: 10.1038/nnano.2013.243; pmid: 24302027
12. D. Foster *et al.*, Two-dimensional skyrmion bags in liquid crystals and ferromagnets. *Nat. Phys.* **15**, 655–659 (2019). doi: 10.1038/s41567-019-0476-x
13. X. Z. Yu *et al.*, Real-space observation of a two-dimensional skyrmion crystal. *Nature* **465**, 901–904 (2010). doi: 10.1038/nature09124; pmid: 20559382
14. H. Kedia, D. Foster, M. R. Dennis, W. T. M. Irvine, Weaving knotted vector fields with tunable helicity. *Phys. Rev. Lett.* **117**, 274501 (2016). doi: 10.1103/PhysRevLett.117.274501; pmid: 28084747
15. H. A. Atwater, The promise of plasmonics. *Sci. Am.* **296**, 56–63 (2007). doi: 10.1038/scientificamerican0407-56; pmid: 17479631
16. S. Tsesses *et al.*, Optical skyrmion lattice in evanescent electromagnetic fields. *Science* **361**, 993–996 (2018). doi: 10.1126/science.aau0227; pmid: 30026318
17. L. Du, A. Yang, A. V. Zayats, X. Yuan, Deep-subwavelength features of photonic skyrmions in a confined electromagnetic field with orbital angular momentum. *Nat. Phys.* **15**, 650–654 (2019). doi: 10.1038/s41567-019-0487-7

18. S. Tsesses, K. Cohen, E. Ostrovsky, B. Gjonaj, G. Bartal, Spin-Orbit Interaction of Light in Plasmonic Lattices. *Nano Lett.* **19**, 4010–4016 (2019). doi: 10.1021/acs.nanolett.9b01343; pmid: 31046293
19. B. le Feber, N. Rotenberg, D. M. Beggs, L. Kuipers, Simultaneous measurement of nanoscale electric and magnetic optical fields. *Nat. Photonics* **8**, 43–46 (2013). doi: 10.1038/nphoton.2013.323
20. N. Rotenberg, L. Kuipers, Mapping nanoscale light fields. *Nat. Photonics* **8**, 919–926 (2014). doi: 10.1038/nphoton.2014.285
21. B. le Feber, J. E. Sipe, M. Wulf, L. Kuipers, N. Rotenberg, A full vectorial mapping of nanophotonic light fields. *Light Sci. Appl.* **8**, 28 (2019). doi: 10.1038/s41377-019-0124-3; pmid: 30854200
22. G. X. Ni *et al*., Ultrafast optical switching of infrared plasmon polaritons in high-mobility graphene. *Nat. Photonics* **10**, 244–247 (2016). doi: 10.1038/nphoton.2016.45
23. P. Kahl *et al*., Normal-Incidence Photoemission Electron Microscopy (NI-PEEM) for Imaging Surface Plasmon Polaritons. *Plasmonics* **9**, 1401–1407 (2014). doi: 10.1007/s11468-014-9756-6
24. P. Kahl *et al*., Direct Observation of Surface Plasmon Polariton Propagation and Interference by Time-Resolved Imaging in Normal-Incidence Two Photon Photoemission Microscopy. *Plasmonics* **13**, 239–246 (2018). doi: 10.1007/s11468-017-0504-6
25. G. Spektor *et al*., Revealing the subfemtosecond dynamics of orbital angular momentum in nanoplasmonic vortices. *Science* **355**, 1187–1191 (2017). doi: 10.1126/science.aaj1699; pmid: 28302854
26. B. Frank *et al*., Short-range surface plasmonics: Localized electron emission dynamics from a 60-nm spot on an atomically flat single-crystalline gold surface. *Sci. Adv.* **3**, e1700721 (2017). doi: 10.1126/sciadv.1700721; pmid: 28706994
27. D. Podbiel, P. Kahl, F.-J. Meyer zu Heringdorf, Analysis of the contrast in normal-incidence surface plasmon photoemission microscopy in a pump–probe experiment with adjustable polarization. *Appl. Phys. B* **122**, 90 (2016). doi: 10.1007/s00340-016-6363-6
28. D. Podbiel *et al*., Imaging the Nonlinear Plasmoemission Dynamics of Electrons from Strong Plasmonic Fields. *Nano Lett.* **17**, 6569–6574 (2017). doi: 10.1021/acs.nanolett.7b02235; pmid: 28945435
29. T. J. Davis *et al*., Subfemtosecond and Nanometer Plasmon Dynamics with Photoelectron Microscopy: Theory and Efficient Simulations. *ACS Photonics* **4**, 2461–2469 (2017). doi: 10.1021/acsphotonics.7b00676
30. M. Berry, M. Dennis, Polarisation singularities in isotropic random vector waves. *Proc. R. Soc. London Ser. A* **457**, 141–155 (2001). doi: 10.1098/rspa.2000.0660
31. B. Radha, M. Arif, R. Datta, T. K. Kundu, G. U. Kulkarni, Movable Au microplates as fluorescence enhancing substrates for live cells. *Nano Res.* **3**, 738–747 (2010). doi: 10.1007/s12274-010-0040-6
32. Y. O. Nakamura, Spin quantum number of surface plasmon. *Solid State Commun.* **39**, 763–765 (1981). doi: 10.1016/0038-1098(81)90453-1
33. K. Y. Bliokh, A. Y. Bekshaev, F. Nori, Extraordinary momentum and spin in evanescent waves. *Nat. Commun.* **5**, 3300 (2014). doi: 10.1038/ncomms4300; pmid: 24598730
34. K. Y. Bliokh, F. J. Rodriguez-Fortuno, F. Nori, A. V. Zayats, Spin-orbit interactions of light. *Nat. Photonics* **9**, 796–808 (2015). doi: 10.1038/nphoton.2015.201
35. W. Koshibae, N. Nagaosa, Theory of antiskyrmions in magnets. *Nat. Commun.* **7**, 10542 (2016). doi: 10.1038/ncomms10542; pmid: 26821932
36. H. S. Park *et al*., Observation of the magnetic flux and three-dimensional structure of skyrmion lattices by electron holography. *Nat. Nanotechnol.* **9**, 337–342 (2014). doi: 10.1038/nnano.2014.52; pmid: 24727689
37. I. Kézsmárki *et al*., Néel-type skyrmion lattice with confined orientation in the polar magnetic semiconductor GaV_4S_8. *Nat. Mater.* **14**, 1116–1122 (2015). doi: 10.1038/nmat4402; pmid: 26343913
38. S. Heinze *et al*., Spontaneous atomic-scale magnetic skyrmion lattice in two dimensions. *Nat. Phys.* **7**, 713–718 (2011). doi: 10.1038/nphys2045
39. A. K. Nayak *et al*., Magnetic antiskyrmions above room temperature in tetragonal Heusler materials. *Nature* **548**, 561–566 (2017). doi: 10.1038/nature23466; pmid: 28846999
40. G. H. Yuan, N. I. Zheludev, Detecting nanometric displacements with optical ruler metrology. *Science* **364**, 771–775 (2019). doi: 10.1126/science.aaw7840; pmid: 31072905
41. G. Yuan, E. T. F. Rogers, N. I. Zheludev, "Plasmonics" in free space: Observation of giant wavevectors, vortices, and energy backflow in superoscillatory optical fields. *Light Sci. Appl.* **8**, 2 (2019). doi: 10.1038/s41377-018-0112-z; pmid: 30622705
42. F. J. García de Abajo, Microscopy: Photons and electrons team up. *Nature* **462**, 861 (2009). doi: 10.1038/462861a; pmid: 20016589
43. B. Barwick, D. J. Flannigan, A. H. Zewail, Photon-induced near-field electron microscopy. *Nature* **462**, 902–906 (2009). doi: 10.1038/nature08662; pmid: 20016598
44. A. Polman, M. Kociak, F. J. García de Abajo, Electron-beam spectroscopy for nanophotonics. *Nat. Mater.* **18**, 1158–1171 (2019). doi: 10.1038/s41563-019-0409-1; pmid: 31308514

ACKNOWLEDGMENTS

Funding: We acknowledge support from the ERC (Complexplas, 3DPrintedoptics), DFG (SPP1391 Ultrafast Nanooptics, CRC 1242 "Non-Equilibrium Dynamics of Condensed Matter in the Time Domain" project no. 278162697-SFB 1242), BMBF (Printoptics), BW Stiftung (Spitzenforschung, Opterial), Carl-Zeiss Stiftung, IQST, and MPI FKF for a visiting guest professorship to T.J.D. **Author contributions:** T.J.D. and F.-J.M.z.H. conceived the idea of polarization projection; D.J., P.D., and F.-J.M.z.H set up the polarization control and carried out the PEEM experiment; T.J.D. carried out the simulations, the vectorial retrieval, and the skyrmion number analysis; B.F. and H.G. grew the single-crystalline gold flakes and carried out ion beam structuring; H.G. conceived the skyrmion vector dynamics idea; T.J.D. and H.G. wrote the manuscript; and all authors contributed to discussions and final editing. **Competing interests:** All authors declare no competing interests. **Data and materials availability:** All data needed to evaluate the conclusions in the paper are present in the paper or the supplementary materials.

SUPPLEMENTARY MATERIALS

science.sciencemag.org/content/368/6489/eaba6415/suppl/DC1
Supplementary Text
Figs. S1 to S5
References (45–47)
Movies S1 to S7

20 December 2019; accepted 12 March 2020
10.1126/science.aba6415

Science

Ultrafast vector imaging of plasmonic skyrmion dynamics with deep subwavelength resolution

Timothy J. Davis, David Janoschka, Pascal Dreher, Bettina Frank, Frank-J. Meyer zu Heringdorf and Harald Giessen

Science **368** (6489), eaba6415.
DOI: 10.1126/science.aba6415

Watching plasmonic skyrmions

Skyrmions are stable topological textures that arise from solutions of the electromagnetic field. Because these "hedgehog"-like textures are robust, can be manipulated, and can interact, there is an interest in pursuing them for memory and logic applications. Skyrmions can also be generated in thin metal layers under optical excitation, but detailed information about the vectorial dynamics of these surface plasmon polariton skyrmions is so far lacking. Davis *et al.* used a time-resolved photoelectron vector microscope to image their spatiotemporal dynamics, piecing together movies as the skyrmions propagated across the surface of a perfect gold crystal. Access to dynamics with such high spatial and temporal resolution could help in controlling other nanophotonic systems.

Science, this issue p. eaba6415